Received: 24 May 2021 | Revised: 6 August 2021 | Accepted: 3 September 2021

IET Generation, Transmission & Distribution

DOI: 10.1049/gtd2.12297

The Institution of Engineering and Technology WILEY

ORIGINAL RESEARCH PAPER

An enhanced predictive hierarchical power management framework for islanded microgrids

Jimiao Zhang[1] | **Jie Li**[1] | **Ning Wang**[2] | **Ben Wu**[1]

[1] Department of Electrical and Computer Engineering, Rowan University, Glassboro, New Jersey, USA

[2] Department of Computer Science, Rowan University, Glassboro, New Jersey, USA

Correspondence
Jie Li, Department of Electrical and Computer Engineering, Rowan University, Glassboro, NJ 08028, USA.
Email: lijie@rowan.edu

Funding information
NSF Division of Electrical, Communications and Cyber Systems, Grant/Award Number: 1952683

Abstract

This paper proposes an enhanced three-layer predictive hierarchical power management framework for secure and economic operation of islanded microgrids. The tertiary control, guaranteeing the microgrid economic operation, is built upon the semi-definite programming-based AC optimal power flow model, which periodically sends power references to secondary control. To mitigate uncertainties arising from renewable generations and loads, a centralized linear model predictive control (MPC) controller is proposed and implemented for secondary control. The MPC controller can effectively regulate the microgrid system frequency by closely tracking reference signals from the tertiary controller with low computational complexity. Droop-based primary controllers are implemented to coordinate with the secondary MPC controller to balance the system in real time. Both synchronous generators (SGs) and solar photovoltaics (PVs) are simulated in the microgrid power management framework. A unified linear input-state estimator (ULISE) is proposed for SG state variable estimation and control anomaly detection due to compromised cyber-physical system components, etc. Simulation results demonstrated that SG states can be accurately estimated, while inconsistency in control signals can be effectively detected for an enhanced MPC. Furthermore, comparing with conventional proportional-integral (PI) control, the proposed hierarchical power management scheme exhibits superior frequency regulation capability whilst maintaining lower system operating costs.

1 | INTRODUCTION

The microgrid hierarchical control [1–2] has been studied for a decade, inspired by the bulk power systems operation framework. The system control architecture is commonly divided into three layers: primary, secondary, and tertiary. The primary control takes care of instantaneous system fluctuations due to loads and renewable energy sources (RESs) and allows for a real-time power balancing and sharing among distributed generators (DGs). Primary control commonly relies on droop control. The secondary control eliminates the steady-state frequency and voltage deviations caused by real-time primary control [3]. The tertiary control is responsible for economic dispatch (ED) and reactive power control to manage power flows. Two methods are commonly studied in the literature for implementing different control layers: centralized [4,5] and distributed [6–8]. The distributed control has well recognized advantages, including scalability, high reliability without a single point of failure, low communication latency, etc. On the other hand, the centralized control is structurally simpler with guaranteed convergence to the optimal solution. It is pointed out in [3] that centralized control is more suitable for islanded microgrids with critical demand-supply balances and fixed infrastructures, whereas distributed control is a better fit for grid-connected microgrids.

For a stand-alone microgrid with high penetration of renewables, the difficulty to handle the adverse impacts of renewable and load uncertainties on power quality poses a severe challenge to the system's power management. Apart from the commonly observed system frequency and voltage deviations, ED of DGs inside the microgrid may also be compromised due to high uncertainties. To this end, several research works tried to address this challenge using different approaches. One major research is to use mathematical programming, such as stochastic programming (SP) [9,10], robust optimisation (RO) [11–13], or

chance-constrained programming (CCP) [14,15], etc. to model the microgrid system uncertainties. Nonetheless, the performance of these methods is highly constrained by the accuracy of the uncertainty modelling, and they are based on offline open-loop optimization, which may have limited robustness to external disturbance or noise compared with the closed-loop feedback mechanism. Hence, potential performance degradation is commonly criticized in practical applications.

Another stream of research focuses on advanced control strategies such as model predictive control (MPC) [16]. MPC provides an inherent feedback mechanism, which makes the system more robust against uncertainties. Furthermore, the ability of MPC to explicitly incorporate system constraints alongside forecasting information enables a constrained optimal control. The rising popularity of MPC theories has indeed spurred a growing interest in their applications in microgrid power management [17–20]. Velasquez et al. [21] present a single-level distributed MPC for solving the intra-hour ED of a microgrid. The controller keeps adjusting the generation schedules in real time along with updated forecasting. To cope with inevitable forecast errors, a two-level stochastic MPC scheme is proposed in [22] to minimise the discrepancy between the actual energy exchange and the optimally planned one. A supervisory MPC is presented in [23] to ensure reliable and economic operation of islanded hybrid AC/DC microgrids. In [24], a hierarchical predictive controller executes daily scheduling and real-time control of a photovoltaic (PV) microgrid, with energy storage systems (ESSs) and diesel generators making up for the load and RES fluctuations. Among all these MPC-based research, linear MPC is preferred for its capability of dramatically reducing the complexities in controller design and control signal computation. Furthermore, the designed controllers can still provide corrective actions for enhanced system robustness in the presence of disturbances [25,26].

It should be emphasized that the performance of MPC depends highly on the prediction model accuracy, which in turn relies on the current system states. One common assumption in the above works was that the system states are already known or directly measurable when MPC is implemented. However, in an islanded microgrid with low inertia, unpredictable demand responses, and high penetration of renewables, the system states could be extremely volatile, so simply assuming a given system state is not rational in practice. In addition, state variables of conventional synchronous generators (SGs), such as rotor angle and field winding voltage, cannot be directly measured in practice [27–29]. Besides, cyber-physical microgrid systems are becoming increasingly vulnerable to extreme weather events, component outages, and cyber-physical attacks [30], which are collectively defined as anomalies in our work. These anomalies may lead to unreliable transmission of sensor measurements and control signals. Although the Kalman filter can detect anomalies in sensor readings by means of analytical redundancy [31] and also estimate unmeasurable system states [32], it is unable to detect such anomalies in control signals manipulation. Lastly, many MPC-based approaches, e.g., [17] and [21], employed static system models for the secondary control, following the convention of the bulk power systems that this control level is implemented on the timescale of minutes. However, a microgrid system with high penetrations of RESs and flexible loads presents much higher system frequency and/or power fluctuations, and forecasting errors of load and renewables will quickly go up when the secondary control of a longer period is implemented. Thus, in order to simultaneously track the economic operation setpoints from the tertiary controller and to react to these high fluctuations, it is desired for the secondary controller to operate in shorter time control intervals (i.e. several seconds) using near real-time forecasting techniques with lower prediction errors. Furthermore, unlike power electronics converters whose dynamics may decay quickly in several milliseconds, conventional DGs such as electrically excited SGs have relatively slow dynamics that cannot be ignored on the timescale of a few seconds. Hence, a dynamic system model would be favoured on this timescale. All these identified research gaps are explored and filled in this work.

In this paper, an enhanced predictive hierarchical power management framework is proposed for islanded microgrids as shown in Figure 1. AC optimal power flow (AC-OPF) is implemented as the tertiary controller to set the reference values for the secondary and the primary level controllers. Given the dynamics decoupling with the secondary control and also the fact that forecasting error goes down with shorter time scale, AC-OPF takes load and renewable forecasts in tens of seconds and executes in the same time frame. The AC-OPF problem per se is nonlinear and nonconvex due to the quadratic relationship between voltages and active/reactive power injections, and thus hard to obtain a global optimum efficiently. The AC-OPF implemented in the proposed power management framework is based on the authors' previous works on semi-definite programming (SDP) [33–34] for global optimal solutions with guaranteed computational performance [35]. Generally, a microgrid with high renewable integration necessitates sufficient reactive power support, without which voltage instability may occur during system operation. Static var compensators (SVCs) or static synchronous compensators (STATCOMs) are used to underpin the reactive power compensation in our simulated system, with voltage references V_{ref} periodically derived from the AC-OPF module and applied to the SG excitation systems to regulate their terminal voltages.

The secondary control is implemented via a linear MPC controller responsible for system frequency regulation and active power control in the time frame of several seconds. During each control time interval, MPC will generate an optimal control trajectory by solving an optimization problem over an extended time frame, whereas only the solution to the first control time interval will be used for actual control. The proposed MPC controller is built on a linearized system model (also known as prediction model) that is updated at run time to account for nonlinearity and time-varying system states. The MPC controller makes sequential control decisions based on the system state estimation via a unified linear input-state estimator (ULISE) [36], while taking renewable forecasts within a receding horizon. In addition, the proposed ULISE can simultaneously estimate the secondary control signals actually received by the primary

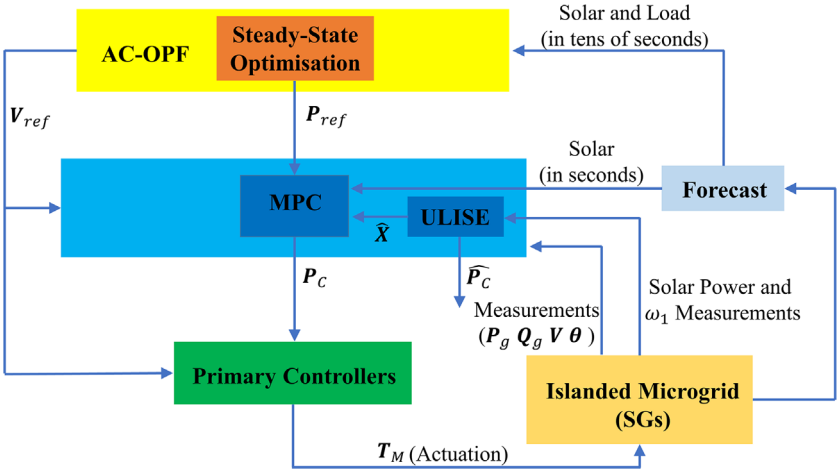

FIGURE 1 Overall block diagram of the proposed hierarchical power management framework

controllers from MPC. Thus, whether the control signals sent from the secondary MPC controller are successfully received by the primary controller without being compromised could be effectively identified. With this, not only the system observability but also the situational awareness can be greatly enhanced. The primary controllers consist of the excitation and turbine-governor systems, receiving the voltage references from AC-OPF and power settings from MPC, respectively.

The major contributions of this paper are summarized as

1. Core system operational functions, i.e., frequency regulation, optimal power flow, and state estimation are systematically integrated and coordinated via an enhanced predictive hierarchical power management framework for the economic and secure operation of islanded microgrids.
2. A linear MPC controller is proposed for the secondary control, built upon a linearized dynamic system model that is periodically updated at runtime for uncertainty mitigation, which is highly responsive to system frequency fluctuations and renewable power variations.
3. An optimal recursive filter (ULISE) is proposed for joint estimation of system states and control signals received by primary controllers in an unbiased minimum-variance (UMV) sense for enhanced MPC capability.

The remainder of this paper is organized as follows: Section 2 presents the mathematical modelling of an islanded microgrid. Section 3 introduces the detailed MPC problem formulation for secondary control. Time-domain simulations via MATLAB/Simulink are rigorously conducted in Section 4 to evaluate the effectiveness of the proposed hierarchical power management framework. Conclusions and future work are presented in Section 5.

2 | MICROGRID SYSTEM MODELLING

An islanded microgrid with dispatchable SGs and intermittent solar PVs is modelled based on a practical microgrid system. The PVs are operated in the maximum power point tracking (MPPT) mode. SGs, loads, or PV arrays connected to the same bus are aggregated. The modeled microgrid consists of N_G aggregated SGs, N_{PV} aggregated PV arrays, N_D aggregated loads, N_l lines, and N_b buses. The first N_G buses are generator buses, with the rest being load buses.

2.1 | Microgrid component modelling

2.1.1 | Synchronous generator model

Given the trade-off between model accuracy and computation speed, the simplified third-order one-axis model (1–3) is used to represent the SG at bus i for its good dynamic decryption [37], assuming that the direct-axis component of the internal voltage behind the transient reactance has vanished and that each SG is installed with a non-reheat steam turbine and a fast excitation system.

$$\dot{\delta}_i = \omega_i - \omega_{com} \tag{1}$$

$$\dot{\omega}_i = \frac{T_{Mi}}{M_i} - \frac{E'_{qi} I_{qi}}{M_i} - \frac{\left(X_{qi} - X'_{di}\right)}{M_i} I_{di} I_{qi} - \frac{D_i\left(\omega_i - \omega_{com}\right)}{M_i} \tag{2}$$

$$\dot{E}'_{qi} = -\frac{E'_{qi}}{T'_{doi}} - \frac{\left(X_{di} - X'_{di}\right)}{T'_{doi}} I_{di} + \frac{E_{fdi}}{T'_{doi}} \tag{3}$$

where ω_{com} is the angular velocity of the common reference frame conventionally chosen as the nominal synchronous speed ω_s in a large system [38]. It is allowed to deviate from the nominal frequency in the context of islanded microgrids. M_i denotes the constant $\frac{2H_i}{\omega_s}$, and time is in seconds. Since the governor dynamics usually dies out much faster than the turbine dynamics [39], the governor valve position is not considered as a state variable. Each SG is expressed in a direct-quadrature (d-q) reference frame rotating with its rotor.

The overall high-gain static excitation system model of the SG is:

$$\dot{E}_{fdi} = -\frac{E_{fdi}}{T_{Ai}} + \frac{K_{Ai}\left(V_{\text{ref},i} - V_i\right)}{T_{Ai}} \tag{4}$$

The turbine-governor model of the SG is:

$$\dot{T}_{Mi} = -\frac{T_{Mi}}{T_{CHi}} + \frac{P_{Ci}}{T_{CHi}} - \frac{1}{R_{Di}T_{CHi}}\left(\frac{\omega_i}{\omega_s} - 1\right) \tag{5}$$

For the SG at bus i, its stator voltage equations are:

$$V_i \sin\left(\delta_i - \theta_i\right) + R_{si}I_{di} - X_{qi}I_{qi} = 0 \tag{6}$$

$$V_i \cos\left(\delta_i - \theta_i\right) + R_{si}I_{qi} + X'_{di}I_{di} - E'_{qi} = 0 \tag{7}$$

The active/reactive power outputs of the SG when the stator resistance is neglected are:

$$P_{gi} = X_{qi}I_{di}I_{qi} + I_{qi}\left(E'_{qi} - X'_{di}I_{di}\right) \tag{8}$$

$$Q_{gi} = -X_{qi}I_{qi}^2 + I_{di}\left(E'_{qi} - X'_{di}I_{di}\right) \tag{9}$$

2.1.2 | PV model

The PV array is modelled as a controlled AC current source operating with time-varying power generations at unity power factor.

2.1.3 | Load model

A static ZIP load (10,11) is modelled:

$$P_{Di} = P_{Dni}\left(a_{1i}V_i^2 + a_{2i}V_i + a_{3i}\right) \tag{10}$$

$$Q_{Di} = Q_{Dni}\left(b_{1i}V_i^2 + b_{2i}V_i + b_{3i}\right) \tag{11}$$

where n signifies the nominal value of the aggregated load at bus i. Each load is comprised of constant impedance (Z), constant current (I), and constant power (P) components. The coefficients a_{1i} to a_{3i} and b_{1i} to b_{3i} define the proportions of each component.

2.1.4 | Network model

The nominal π model is used for the microgrid network modelling, with power balance for bus i shown in (12,13):

$$I_{di}V_i \sin\left(\delta_i - \theta_i\right) + I_{qi}V_i \cos\left(\delta_i - \theta_i\right) + P_{PVi} - P_{Di} = \sum_{j=1}^{N_b} V_iV_jY_{ij} \cos\left(\theta_i - \theta_j - \alpha_{ij}\right) \tag{12}$$

$$I_{di}V_i \cos\left(\delta_i - \theta_i\right) - I_{qi}V_i \sin\left(\delta_i - \theta_i\right) + Q_{PVi} - Q_{Di} = \sum_{j=1}^{N_b} V_iV_jY_{ij} \sin\left(\theta_i - \theta_j - \alpha_{ij}\right) \tag{13}$$

where α_{ij} and Y_{ij} denote the angle and magnitude of the ij^{th} element of the bus admittance matrix $\mathbf{Y}_b$, respectively. The corresponding terms will be zero when a grid component is absent from the above two equations.

2.2 | Linearisation of microgrid system model

Linearisation of the above differential-algebraic equations (DAEs) that model the microgrid system lays the foundation for the design of the secondary MPC controller. Since the d-q coordinates of each SG should have a reference angle, we define all the SG and bus angles relative to the rotor angle of the SG at bus 1 as

$$\begin{aligned} \delta'_i &= \delta_i - \delta_1 \qquad i = 1, \ldots, N_G \\ \theta'_i &= \theta_i - \delta_1 \qquad i = 1, \ldots, N_b \end{aligned} \tag{14}$$

Below vectors of state variables ΔX, output variables $\Delta \boldsymbol{Y}$ etc. are defined:

$$\begin{aligned} \Delta X &= [\Delta\delta'_1, \Delta\omega_1, \Delta E'_{q1}, \Delta E_{fd1}, \Delta T_{M1}, \ldots, \Delta E_{fdN_G}, \Delta T_{MN_G}] \\ \Delta \mathrm{Y} &= [\Delta P_{g1}, \Delta Q_{g1}, \ldots, \Delta P_{gN_G}, \Delta Q_{gN_G}] \\ \Delta \mathrm{I}_g &= [\Delta I_{d1}, \Delta I_{q1}, \ldots, \Delta I_{dN_G}, \Delta I_{qN_G}]^T \\ \Delta \mathrm{V}_g &= [\Delta\theta'_1, \Delta V_1, \ldots, \Delta\theta'_{N_G}, \Delta V_{N_G}]^T \\ \Delta \boldsymbol{V}_l &= [\Delta\theta'_{N_G+1}, \Delta V_{N_G+1}, \ldots, \Delta\theta'_{N_b}, \Delta V_{N_b}]^T \\ \Delta \boldsymbol{U}_c &= [\Delta \boldsymbol{U}_1^T, \Delta \boldsymbol{U}_2^T]^T \end{aligned}$$

where $\Delta \boldsymbol{U}_1 = [\Delta\omega_1, \Delta V_{ref1}, \Delta V_{ref2}, \ldots, \Delta V_{refN_G}]^T$ and

$$\begin{aligned} \Delta \boldsymbol{U}_2 &= [\Delta P_{C1}, \Delta P_{C2}, \ldots, \Delta P_{CN_G}]^T \\ \Delta \boldsymbol{S}_{1PV} &= [\Delta P_{PV1}, \Delta Q_{PV1}, \ldots, \Delta P_{PVN_G}, \Delta Q_{PVN_G}]^T \\ \Delta \boldsymbol{S}_{2PV} &= \left[\Delta P_{PVN_G+1}, \Delta Q_{PVN_G+1}, \ldots, \Delta P_{PVN_b}, \Delta Q_{PVN_b}\right]^T \end{aligned} \tag{15}$$

Linearisation of (1–5) leads to the compact form (16):

$$\Delta \dot{\boldsymbol{X}} = \boldsymbol{A}_1\Delta \boldsymbol{X} + \boldsymbol{B}_1\Delta \boldsymbol{I}_g + \boldsymbol{B}_2\Delta \boldsymbol{V}_g + \boldsymbol{E}_1\Delta \boldsymbol{U}_c \tag{16}$$

where $[\boldsymbol{A}_1]_{(5N_G \times 5N_G)}$, $[\boldsymbol{B}_1]_{(5N_G \times 2N_G)}$ and $[\boldsymbol{B}_2]_{(5N_G \times 2N_G)}$ are block diagonal matrices.

Linearising (6,7) yields the augmented form of (17):

$$\boldsymbol{C}_1\Delta \boldsymbol{X} + \boldsymbol{D}_1\Delta \boldsymbol{I}_g + \boldsymbol{D}_2\Delta \boldsymbol{V}_g = 0 \tag{17}$$

where $[\boldsymbol{C}_1]_{(2N_G \times 5N_G)}$, $[\boldsymbol{D}_1]_{(2N_G \times 2N_G)}$, and $[\boldsymbol{D}_2]_{(2N_G \times 2N_G)}$ are block diagonal matrices.

Linearizing the network Equations (12–13) of generator buses yields:

$$\boldsymbol{C}_2\Delta\boldsymbol{X} + \boldsymbol{D}_3\Delta\boldsymbol{I}_g + \boldsymbol{D}_4\Delta\boldsymbol{V}_g + \boldsymbol{D}_5\Delta\boldsymbol{V}_l + \boldsymbol{F}_1\Delta\boldsymbol{S}_{1PV} = 0 \quad (18)$$

where $[\boldsymbol{C}_2]_{(2N_G\times 5N_G)}$ and $[\boldsymbol{D}_3]_{(2N_G\times 2N_G)}$ are block diagonal matrices, $[\boldsymbol{D}_4]_{(2N_G\times 2N_G)}$ and $[\boldsymbol{D}_5]_{(2N_G\times 2(N_b-N_G))}$ are full matrices, and $[\boldsymbol{F}_1]_{(2N_G\times 2N_G)}$ is a sparse incidence matrix with diagonal entries of 1 if a PV is present on the corresponding bus.

Likewise, for load buses, (12–13) are linearized as

$$\boldsymbol{D}_6\Delta\boldsymbol{V}_g + \boldsymbol{D}_7\Delta\boldsymbol{V}_l + \boldsymbol{F}_2\Delta\boldsymbol{S}_{2PV} = 0 \quad (19)$$

where $[\boldsymbol{D}_6]_{(2(N_b-N_G)\times 2N_G)}$ and $[\boldsymbol{D}_7]_{(2(N_b-N_G)\times 2(N_b-N_G))}$ are full matrices, and $[\boldsymbol{F}_2]_{(2(N_b-N_G)\times 2(N_b-N_G))}$ is a sparse incidence matrix with entries either 0 or 1. ΔQ_{PV} at all buses is 0 since PV is modelled at unity power factor.

$\Delta\boldsymbol{I}_g$ in (16) and (18) is eliminated via (17). Then $\boldsymbol{E}_1$in (16) could be partitioned as $\boldsymbol{E}_{11}$ and $\boldsymbol{E}_{12}$ according to $\Delta\boldsymbol{U}_1$ and $\Delta\boldsymbol{U}_2$, and $[\Delta\boldsymbol{V}_g^T\ \Delta\boldsymbol{V}_l^T]^T$is further eliminated. After some algebra, $\boldsymbol{E}_{11}$ is contained in a new matrix $\boldsymbol{B}_{sys}$ and the linearized state equations could be represented as (20) based on (16–19):

$$\Delta\dot{\boldsymbol{X}} = \boldsymbol{A}_{sys}\Delta\boldsymbol{X} + \boldsymbol{B}_{sys}\Delta\boldsymbol{S} + \boldsymbol{E}_{12}\Delta\boldsymbol{U}_2 \quad (20)$$

where$\Delta\boldsymbol{S} := [\Delta\boldsymbol{U}_1^T\ \Delta\boldsymbol{S}_{PV}^T]^T$ and $\Delta\boldsymbol{S}_{PV} := [\Delta\boldsymbol{S}_{1PV}^T\ \Delta\boldsymbol{S}_{2PV}^T]^T$.

Similarly, after $\Delta\boldsymbol{I}_g$ is eliminated from the linearized form of (8–9), the system output equations result:

$$\Delta\boldsymbol{Y} = \boldsymbol{C}_{\text{sys}}\Delta\boldsymbol{X} + \boldsymbol{D}_{\text{sys}}\Delta\boldsymbol{S} \quad (21)$$

The linear time-varying microgrid system modelled as (20) and (21) is discretized for digital control. In what follows, the subscripts are dropped, and the discretized system model is formulated as

$$\Delta\boldsymbol{X}(k+1) = \boldsymbol{A}\Delta\boldsymbol{X}(k) + \boldsymbol{B}\Delta\boldsymbol{S}(k) + \boldsymbol{E}\Delta\boldsymbol{U}(k) \quad (22)$$

$$\Delta\boldsymbol{Y}(k) = \boldsymbol{C}\Delta\boldsymbol{X}(k) + \boldsymbol{D}\Delta\boldsymbol{S}(k) \quad (23)$$

where $\Delta\boldsymbol{S}(k)$ represents the vector of known inputs, and $\Delta\boldsymbol{U}(k)$ denotes the vector of unknown inputs at time instant k, which are also known as the manipulated inputs in MPC.

3 | MPC PROBLEM FORMULATION

3.1 | Linear MPC controller

Building on the linearized microgrid system model (22,23), a linear centralized MPC controller formulated as (24) is designed to solve a multi-objective quadratic optimisation problem over a prediction horizon. For an islanded microgrid, frequency regulation is of critical significance. Hence, the main goal of the secondary MPC controller is to minimise the accumulated frequency deviations not handled by primary controller (the first component of (24.1)), whilst managing the generation dispatch of SGs following the set-points from tertiary controller (the second component of (24.1)).

$$\min \sum_{k=1}^{N_p} \Big[\Delta_s\boldsymbol{\omega}(t+k|t)^T\boldsymbol{G}\Delta_s\boldsymbol{\omega}(t+k|t) + \Delta_n\boldsymbol{P}_g(t+k|t)^T\boldsymbol{H}\Delta_n\boldsymbol{P}_g(t+k|t)\Big] + \rho_\epsilon\epsilon^2 \quad (24.1)$$

$$s.t.\ \Delta\boldsymbol{X}(t+k|t) = \boldsymbol{A}\Delta\boldsymbol{X}(t+k-1|t) + \boldsymbol{B}\Delta\boldsymbol{S}(t+k-1|t) + \boldsymbol{E}\Delta\boldsymbol{U}(t+k|t) \quad (24.2)$$

$$\Delta\boldsymbol{Y}(t+k|t) = \boldsymbol{C}\Delta\boldsymbol{X}(t+k|t) + \boldsymbol{D}\Delta\boldsymbol{S}(t+k|t) \quad (24.3)$$

$$0.99\omega_s \le \Delta\omega_i(t+k|t) + \omega_i(t) \le 1.01\omega_s \quad (24.4)$$

$$U_i^{min} \le \Delta U_i(t+k|t) + U_i(t) \le U_i^{max} \quad (24.5)$$

$$Y_i^{min} - \epsilon 1 \le \Delta Y_i(t+k|t) + Y_i(t) \le Y_i^{max} + \epsilon 1 \quad (24.6)$$

where t refers to the current control time instant, and the duration of each control interval is T_c. k denotes the k^{th} control interval; N_p is the prediction horizon defined as the number of T_c the MPC executes for forward-looking purposes. N_c, a portion of N_p, is defined as the control horizon such that $\Delta\boldsymbol{U}(t+j) = \Delta\boldsymbol{U}(t+N_c)$ for $j \in [N_c+1,\ N_p]$. The reason for introducing N_c is to reduce the number of control variables for faster computational speed whilst avoiding potential numerical issues. $\Delta_s\boldsymbol{\omega} := [\Delta_s\omega_1, \Delta_s\omega_2 \dots, \Delta_s\omega_m]^T/\omega_s$ is the normalized vector of the rotor speed deviations from $\boldsymbol{\omega}_s$, and $\Delta_n\boldsymbol{P}_g := [\Delta_n P_{g1}, \Delta_n P_{g2} \dots, \Delta_n P_{gm}]^T$ refers to the vector of power output deviations from $\boldsymbol{P}_{\text{ref}}$. For predictions at control time instant $t+k$, $\Delta_s\omega_i(t+k|t) := \Delta\omega_i(t+k|t) + \omega_i(t) - \omega_s$ and $\Delta_n P_{gi}(t+k|t) = \Delta P_{gi}(t+k|t) + P_{gi}(t) - P_{ref,i}$. $\boldsymbol{G} = \text{diag}(g_1, g_2, \dots, g_m)$ and $\boldsymbol{H} = \text{diag}(h_1, h_2, \dots, h_m)$ are diagonal weighting matrices; weights in $\boldsymbol{G}$ are set greater than those in $\boldsymbol{H}$ since frequency regulation is more crucial for an islanded microgrid's secondary control. The first two constraints (24.2) and (24.3) represent the prediction model based on (22,23). The coefficient matrices $\boldsymbol{A}, \boldsymbol{B}, \boldsymbol{E}, \boldsymbol{C}$ and $\boldsymbol{D}$ are updated at each model update period T_s to adapt the prediction model to the varying system operating conditions and are assumed constant over the prediction horizon. The MPC is executed in every control interval over the prediction horizon, based on the updated inputs including the system state, measurements and the PV forecasts. The proposed ULISE works at a higher sampling rate to provide the MPC controller with system state estimations for each control interval, and the rotor speed ω_1 can be obtained using

a simple frequency estimator based on a phasor demodulation principle [27]. Constraint (24.4) requires the rotor speeds to stay within the permissible bounds, i.e., $\pm 1\%\,\omega_s$, whereas (24.5) constrains the manipulated inputs. In (24.6), Y_i^{min} and Y_i^{max} are the vectors representing per unit active and reactive power limits for SG i. The non-negative slack variable ϵ is introduced to relax (24.6), as hard output constraints may cause infeasibility owing to unpredicted disturbances or model mismatch. 1 is a column vector of 1s with dimension 2, whilst the weight ρ_ϵ in the objective function penalizes the violation of this constraint. Micro-synchrophasors could be used to provide the measurements of voltage magnitudes, phase angles, active and reactive powers, allowing us to derive an initial condition of the original nonlinear DAE system by referring to the dynamic circuit of the flux-decay model in [37] such that the numerical simulations can converge fast.

3.2 | ULISE

In order to enhance the performance of the MPC controller, ULISE is proposed to simultaneously estimate the system states and the control signals actually received by primary controllers. This state estimator is built upon the unified filter for general linear discrete-time stochastic systems in [36]. Integrating ULISE into the feedback loop of MPC can effectively reduce the controller sensitivity to output disturbances. Moreover, different from the Kalman filter [29], which can only detect inconsistency in sensor readings through analytical redundancy approaches, the proposed ULISE can also detect compromised control signals, and thus, the capability of the proposed MPC controller and even the system stability could be enhanced. With ULISE, the control signals received by primary controllers could be estimated and compared with the actual control signals sent from MPC controller, and a considerable deviation suggests the presence of anomalies. Mitigation schemes could be further explored to compensate for the error and thus to guarantee the control performance. It should be emphasized that the proposed filter can generate a UMV estimate (that is, the estimated state's variance is the smallest out of all unbiased estimates) when strong detectability is satisfied [36].

For conciseness, the microgrid system model utilized by ULISE within each model update period T_s is rewritten as

$$\boldsymbol{X}_{k+1} = \boldsymbol{A}\boldsymbol{X}_k + \boldsymbol{B}\boldsymbol{S}_k + \boldsymbol{E}\boldsymbol{U}_k + \boldsymbol{w}_k \tag{25}$$

$$\boldsymbol{Y}_k = \boldsymbol{C}\boldsymbol{X}_k + \boldsymbol{D}\boldsymbol{S}_k + \boldsymbol{v}_k \tag{26}$$

Here k refers to the sampling instant of the unified filter. The process noise $\boldsymbol{w}_k \in \mathbb{R}^{5N_G}$ and the measurement noise $\boldsymbol{v}_k \in \mathbb{R}^{2N_G}$ are assumed to be mutually uncorrelated, zero-mean, white random signals with known bounded covariance matrices $\boldsymbol{Q}_k := \mathbb{E}[\boldsymbol{w}_k \boldsymbol{w}_k^T] \geq 0$ and $\boldsymbol{R}_k := \mathbb{E}[\boldsymbol{v}_k \boldsymbol{v}_k^T] \geq 0$. The initial state $\boldsymbol{X}_0$ has mean $\hat{\boldsymbol{X}}_{0|0}$ and covariance $\boldsymbol{P}_{0|0}^{\times}$, and is independent of $\boldsymbol{w}_k$ and $\boldsymbol{v}_k$ for all k. The ULISE is recursively implemented in three steps as shown below: the "Unknown input estimation" uses the current measurements and the state estimates to estimate the unknown inputs in the best linear unbiased sense; the "Time update" propagates the state estimates using the system dynamics, and the "Measurement update" updates the state estimates based on the current measurements.

ULISE algorithm in the case of no direct feedthrough

Initialize: $\hat{\boldsymbol{X}}_{0|0}$, $\boldsymbol{P}_{0|0}^{\times}$ etc.
for $k = 1$ to n_{itr} **do**
▷ Unknown input estimation of $\boldsymbol{U}_{k-1}$
$\tilde{\boldsymbol{P}}_k = \boldsymbol{A}\boldsymbol{P}_{k-1|k-1}^{\times}\boldsymbol{A}^T + \boldsymbol{Q}_{k-1}$
$\tilde{\boldsymbol{R}}_k = \boldsymbol{C}\tilde{\boldsymbol{P}}_k\boldsymbol{C}^T + \boldsymbol{R}_k$
$\boldsymbol{P}_{k-1}^{d} = (\boldsymbol{E}^T\boldsymbol{C}^T\tilde{\boldsymbol{R}}_k^{-1}\boldsymbol{C}\boldsymbol{E})^{-1}$
$\boldsymbol{M}_k = \boldsymbol{P}_{k-1}^{d}\boldsymbol{E}^T\boldsymbol{C}^T\tilde{\boldsymbol{R}}_k^{-1}$
$\hat{\boldsymbol{X}}_{k|k-1} = \boldsymbol{A}\hat{\boldsymbol{X}}_{k-1|k-1} + \boldsymbol{B}\boldsymbol{S}_{k-1}$
$\hat{\boldsymbol{U}}_{k-1} = \boldsymbol{M}_k(\boldsymbol{Y}_k - \boldsymbol{C}\hat{\boldsymbol{X}}_{k|k-1} - \boldsymbol{D}\boldsymbol{S}_k)$
▷ Time update
$\hat{\boldsymbol{X}}_{k|k}^{*} = \hat{\boldsymbol{X}}_{k|k-1} + \boldsymbol{E}\hat{\boldsymbol{U}}_{k-1}$
$\boldsymbol{P}_{k|k}^{*\times} = \boldsymbol{E}\boldsymbol{M}_k\boldsymbol{R}_k\boldsymbol{M}_k^T\boldsymbol{E}^T + (\boldsymbol{I} - \boldsymbol{E}\boldsymbol{M}_k\boldsymbol{C})\tilde{\boldsymbol{P}}_k(\boldsymbol{I} - \boldsymbol{E}\boldsymbol{M}_k\boldsymbol{C})^T$
$\tilde{\boldsymbol{R}}_k^{*} = \boldsymbol{C}\boldsymbol{P}_{k|k}^{*\times}\boldsymbol{C}^T + \boldsymbol{R}_k - \boldsymbol{C}\boldsymbol{E}\boldsymbol{M}_k\boldsymbol{R}_k - \boldsymbol{R}_k\boldsymbol{M}_k^T\boldsymbol{E}^T\boldsymbol{C}^T$
▷ Measurement update
$\boldsymbol{K}_k = \boldsymbol{P}_{k|k}^{*\times}\boldsymbol{C}^T - \boldsymbol{E}\boldsymbol{M}_k\boldsymbol{R}_k$
$\boldsymbol{L}_k = \boldsymbol{K}_k\tilde{\boldsymbol{R}}_k^{*\dagger}$
$\hat{\boldsymbol{X}}_{k|k} = \hat{\boldsymbol{X}}_{k|k}^{*} + \boldsymbol{L}_k(\boldsymbol{Y}_k - \boldsymbol{C}\hat{\boldsymbol{X}}_{k|k}^{*} - \boldsymbol{D}\boldsymbol{S}_k)$
$\boldsymbol{P}_{k|k}^{\times} = \boldsymbol{P}_{k|k}^{*\times} + \boldsymbol{L}_k\tilde{\boldsymbol{R}}_k^{*}\boldsymbol{L}_k^T - \boldsymbol{K}_k\boldsymbol{L}_k^T - \boldsymbol{L}_k\boldsymbol{K}_k^T$
end for

In the above algorithm, n_{itr} refers to the maximum number of iterations for each T_s. All coefficient matrices are updated every T_s, and the covariance matrices of process and measurement noise are assumed to be constant throughout the simulation. $\boldsymbol{P}_{k-1}^{d}$ is covariance matrix of the optimal input error estimates, $\hat{\boldsymbol{U}}_{k-1}$ is unknown input estimates at time instant $k-1$, $\boldsymbol{M}_k$ is filter gain matrix which is chosen to minimise the state and input error covariances, and $\boldsymbol{P}_{k|k}^{*\times}$ represents propagated state estimate error covariance matrix. † denotes the Moore-Penrose pseudoinverse of a matrix [40], and $\boldsymbol{P}_{k|k}^{\times}$ is the updated covariance matrix of state error. The estimated states $\hat{\boldsymbol{X}}_{k|k}$ in the last iteration together with system measurements are used to update the coefficient matrices for the next T_s. In normal conditions, e.g., when no external manipulation is altered, $\hat{\boldsymbol{U}}$ yielded in the first step should be close to zero during each T_s. It is noted that the case in our framework represents a special case of the general ULISE algorithm because there is no direct feedthrough, i.e., the term related to $\boldsymbol{U}_k$ is absent in (26) because the coefficient matrix of $\boldsymbol{U}_k$ is zero. In this regard, no transformation of the output equations and no decomposition of the unknown input vector are necessary. Further, the algorithm will reduce to the conventional Kalman filtering if both the coefficient matrices of $\boldsymbol{U}_k$ in (25) and (26) are empty.

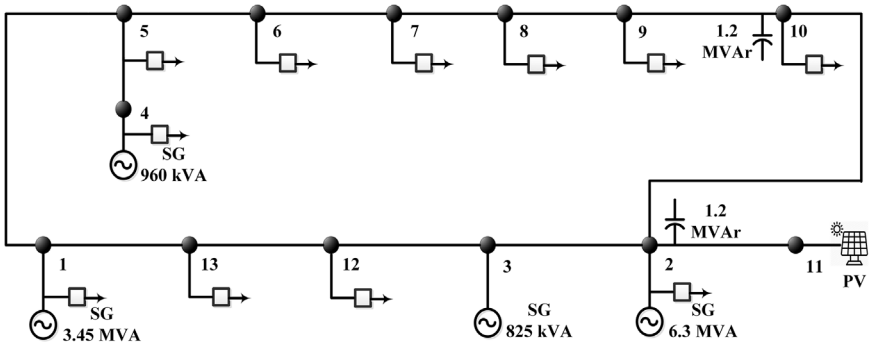

FIGURE 2 Single-line diagram of the islanded microgrid test system

4 | SIMULATION RESULTS

4.1 | Simulation settings

Figure 2 illustrates the single-line diagram of a simulated microgrid built on a 13.2 kV practical distribution network. This 13-bus microgrid connects 11 entities on a dedicated ring. When disconnected from the main grid, these entities are powered by four on-site SGs. Two STATCOMs are installed at buses 2 and 10 for reactive power compensation. Besides, a 2-MW PV farm is integrated into the microgrid at bus 11. The power factor of the ZIP loads ranges from 0.85 to 0.9 lagging, and the total active load of the system is around 8.12 MW. The detailed system parameters are provided in the Appendix. The system base power, voltage, and nominal frequency are set as 10 MVA, 13.2 kV, and 60 Hz, respectively. SGs are simulated using MATLAB/Simulink's existing modules. The components of $\boldsymbol{w}_k$ and $\boldsymbol{v}_k$ in the ULISE are set to be Gaussian random variables with zero mean and standard deviation $\sigma = 10^{-2}$. The initial vector of system states is set as $\hat{\boldsymbol{X}}_{0|0} = 0_{(5m\times1)}$, whilst the covariance matrix of state error is initialized as $\boldsymbol{P}^{x}_{0|0} = \mathrm{diag}([10^{-1}, \ldots, 10^{-1}]_{(5m\times1)})$. The communication latency is neglected considering the microgrid does not span a large geographical area.

All the simulations are run on a PC with an Intel Core i7 at 3.8 GHz, Quad-Core and 64-GB RAM. The MPC controller is designed using the MPC Toolbox in MATLAB. When the controller detects infeasibility, the latest successful control outputs will be retained. Also, the controller will issue a time-out error and terminate the optimization problem if it is not solved within the prescribed control interval. The coordination frequency between ACOPF and MPC has an impact on the overall performance of the proposed control framework. A long coordination period could compromise MPC's power tracking abilities, while a short coordination period may cause greater system frequency deviations at transients. Therefore, it is empirically set that the tertiary control executes ACOPF and updates power set-points every 15 s. The average computational overhead for obtaining an optimal solution to the AC-OPF of the 13-bus system is 0.542 s. During each 15 s, the secondary MPC controller keeps solving the receding optimization problem every T_c over the prediction horizon (N_p of T_c) until the new power references for the next 15 s are received. The choice of control interval and prediction horizon are based on the trade-off between performance and computational effort. In the following tests, $N_p = 5$, $N_c = 3$ and $T_c = 1$ s are chosen. The average computation time per step for this setting is 0.307 s. To capture system dynamics while reducing computational overhead, the model update period T_s is set as 0.02 s and the sampling time for the ULISE is 2 ms in the simulations.

To assist the MPC and ACOPF modules, auto-regressive integrated moving average (ARIMA) models [41] are utilised to provide solar power predictions at different timescales. Specifically, as regards the secondary level, historical solar power outputs with a 1-s sampling rate are used to train the corresponding ARIMA (p, d, q) model, where p denotes the order of auto-regressive (AR), d is the number of nonseasonal differences, and q means the order of moving average (MA). The sample autocorrelation coefficient (ACC) and partial autocorrelation coefficient (PACC) are calculated to determine the nonseasonal differencing before p and q are identified using properly transformed time series. The model orders are determined as (7, 1, 0). This model is utilized at each control interval to predict over the prediction horizon using the last 7 (p) measurements of actual solar power outputs. The model can be regularly trained with new data. As shown in Figure 3, a segment of the actual historical power output of the PV farm in 1 s resolution is used for simulation purposes. The forecasted solar power generated by this ARIMA model is also given. We employ the error metrics defined in [41,42] to evaluate different datasets. With respect to the solar power curve with 1-s resolution, the forecasted curve has a root mean square error (RMSE) of 0.0416 MW and a mean absolute percentage error (MAPE) of 3.84%. Likewise, using the 15-s resolution historical solar power data, an ARIMA (3, 1, 1) model is used to forecast solar power for the ACOPF module; the RMSE and MAPE are found to be 0.1547 MW and 12.41%, respectively.

The total load and system net load (load minus PV output) profiles for the simulations are illustrated in Figure 4.

4.2 | MPC performance evaluation

Case studies are conducted to evaluate the performance of the proposed MPC controller by comparing the transient response and the frequency regulation capacity of the proposed controller

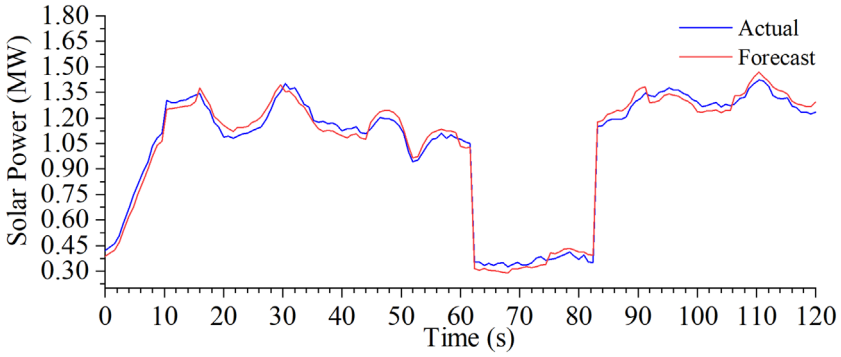

FIGURE 3 Solar power variation curves

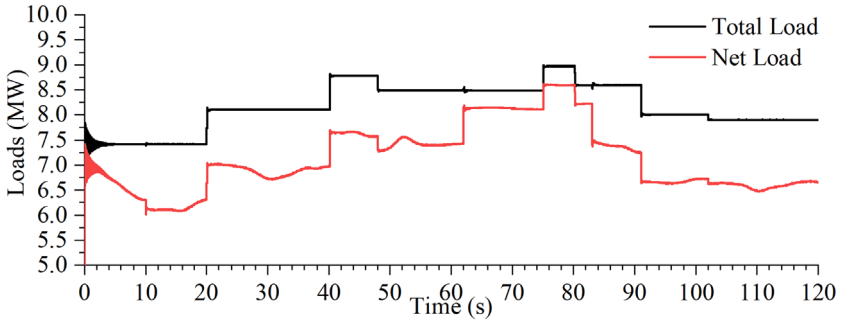

FIGURE 4 Actual total load and net load curves

with a decentralized PI controller proposed in our previous work [34]. In addition, a case where $T_c = 3$ s is also studied to investigate the effect of control intervals on MPC performance. For all the three cases we studied, the AC-OPF and the primary droop controllers remain the same. The control parameters in both controllers are carefully tuned in the MPC Toolbox and the Control System Toolbox of MATLAB, respectively. For comparison purposes, the same set of control parameters and PV forecasts are utilised in the two MPC controllers cases except for the difference in control intervals. As highly oscillatory responses may arise due to the windup of the integrator, which keeps integrating the tracking error even when the output saturates, a clamping technique is adopted for PI [43] to combat such possible effects. The active power outputs of the SGs at buses 1 and 2 regulated by MPC and PI controllers are illustrated in Figure 5 to compare with the references from AC-OPF.

As shown in Figure 5, the MPC controller with a longer control interval, i.e., $T_c = 3$ s, generates slightly smoother SG power outputs than the one with shorter control interval due to less frequent power change settings. In addition, both MPC controllers achieve faster dynamic responses than the PI controller, as shown in the enlarged graphs. Both MPC and PI controllers can track the reference power dispatch signals for SGs from AC-OPF with different tracking errors as a result of imperfect forecasting and controller performance. It is observed that the MPC controllers do not constantly outperform the PI controller. For instance, while the MPC controllers track the active power reference of the SG at bus 2 from $t = 45$ s to $t = 60$ s better, the PI controller beats the MPC controllers from $t = 15$ s to $t = 30$ s for the SG at bus 1. Thus, their power tracking capabilities are further compared in terms of total operating costs, which are determined by the quadratic cost function $(c_{i2} \cdot P_{gi}^2 + c_{i1} \cdot P_{gi} + c_{i0})$ for SG i. In the cost function, c_{i2} ($/(hour · MW^2)), c_{i1} ($/(hour · MW)), and c_{i0} ($/hour) are the quadratic, linear and constant cost coefficients, respectively. The detailed operation cost results are shown in Figure 6. Using the mean bias error (MBE) metric, we find that the proposed MPC controller in the cases of $T_c = 1$ s and $T_c = 3$ s could result in average cost savings of $13.62/h and $12.37/h, respectively, comparing with PI controller. The major operating cost savings happen when the system experiences the highest net load (from t = 63 s to t = 80 s). This is because forecasting information is integrated into the MPC prediction model, allowing the MPC controllers to generate efficient control signals that can lead to more economic operation despite system uncertainty.

The microgrid frequency measurements at bus 6 are presented in Figure 7. Comparing with the well-tuned PI controller, the proposed MPC controller in two control interval settings is able to regulate the microgrid frequency well within the range of 59.4-60.6 Hz and always maintain the microgrid frequency closer to the nominal frequency. Specifically, the mean absolute errors (MAEs) of the frequencies with respect to 60 Hz for MPC with $T_c = 1$ s and $T_c = 3$ s, and PI controllers are 0.1027 Hz, 0.1082 Hz, and 0.1707 Hz, respectively. The main reason for such performance improvement lies in the fact that frequency is rigorously constrained in the MPC model. Additionally, smaller frequency fluctuations, particularly at transients, are observed from the zoomed-in graph when the MPC employs a smaller control interval, enabling the controller to react faster to mitigate the disturbances from solar PV and loads.

Other results related to the case of MPC with $T_c = 1$ s are presented in the rest of this paper as the MPC with $T_c = 3$ s

FIGURE 5 Power tracking for SGs at buses 1 and 2

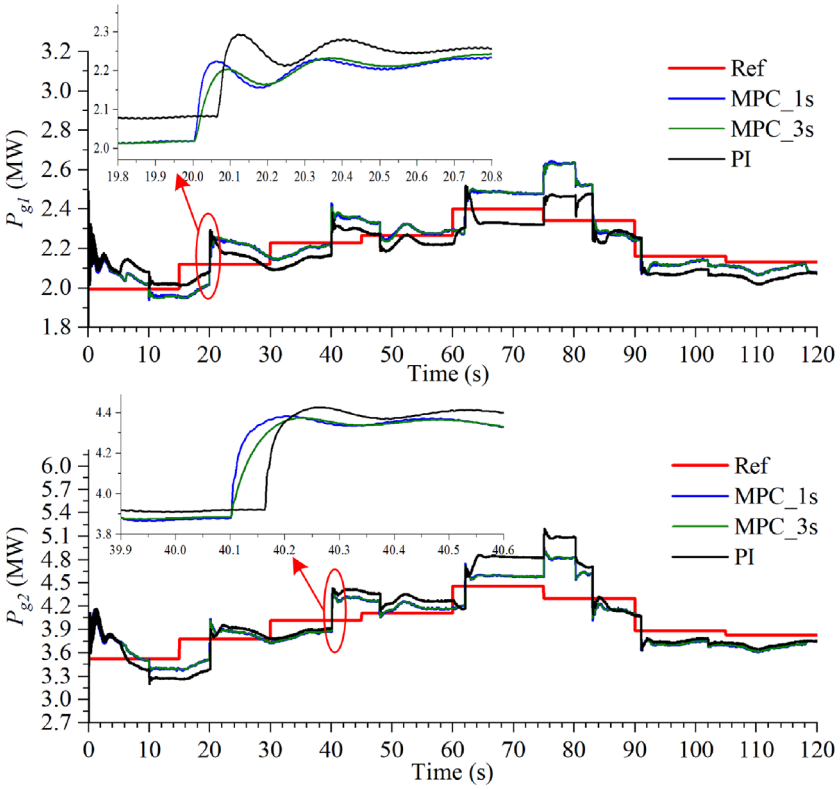

FIGURE 6 Total operating costs

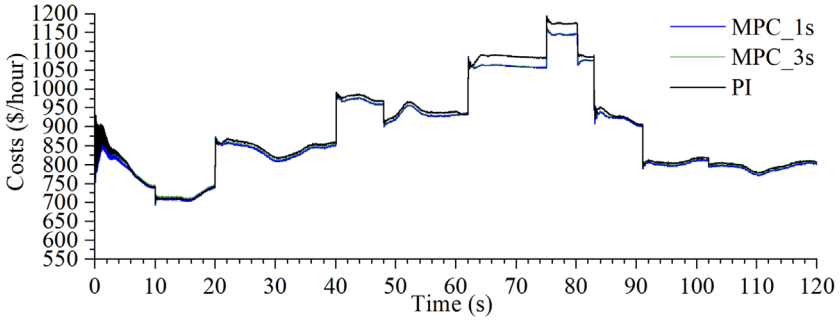

shows similar results. Voltage regulation of the simulated microgrid system is taken care of by the SGs' excitation systems and the STATCOMs. It is observed that voltages at all buses of the simulated system are well regulated within the typical permissible range of 0.95 pu to 1.05 pu, as illustrated in Figure 8 with three sample bus voltages.

The MPC controller is dynamically executed, and eventually brings the system towards a new steady state following any transient, as evidenced above. Figure 9 illustrates the power change settings (P_c), generated by the MPC controller every 1 s and sent to the primary droop controller. It demonstrates that such control signals, during the transient states, are adjusted more aggressively as the operating conditions vary greatly, particularly when the PV plunges at $t = 62$ s. Even at the steady states, adjustments are still being made as a result of the time-varying operating points. Throughout the entire simulation, no time-out error is experienced. However, some identical control signals over multiple consecutive time steps are observed at the transient states, indicating possible constraint violations during these control intervals, which might be attributed to the large model mismatch at transients due to linear approximation.

4.3 | State estimation evaluation

The performance of the proposed MPC controller depends heavily on the state estimation accuracy. The estimated system states $\delta', \omega, E_{fd}, T_M$ from ULISE and their actually recorded signals are presented in Figure 10, which shows that the estimated system states using the proposed ULISE agree closely with the actual signals sampled from the numerical simulation.

In addition, relatively large estimation errors are observed during the transients. These errors are mainly attributed to the low-order approximation in the linear model and the simplified system component models used for state estimation. Nevertheless, these estimates converge quickly to the real values only in

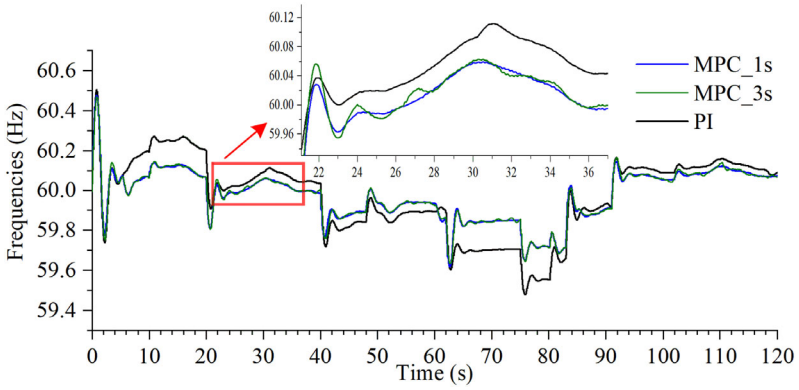

FIGURE 7 System frequencies measured at bus 6

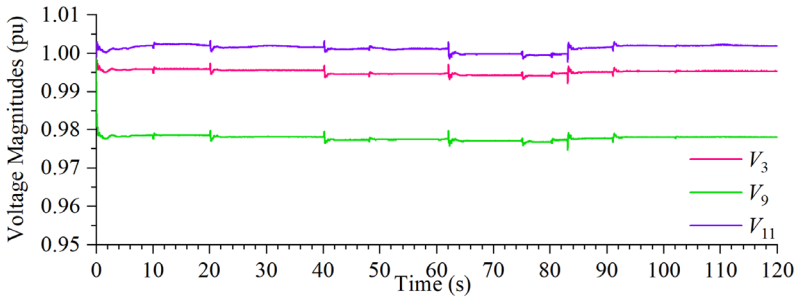

FIGURE 8 Voltage magnitudes at selected buses

a few seconds. Furthermore, over the entire course of time-domain simulations, we kept checking the strong detectability of the linearized microgrid system, without which unbiased state and input estimates cannot be obtained even in the absence of stochastic noise [36]. In the transient states, we also notice that there are a few cases where the strong detectability is not satisfied. That is, the ULISE generates sub-optimal estimates in these scenarios. We believe this is mainly due to the linear approximation of a nonlinear system, and we plan to explore efficient nonlinear filtering to solve this problem in our future work.

4.4 | Anomaly detection using ULISE

To testify the performance of the ULISE in detecting the system anomaly, a scenario where an attacker purposely alters the control signals sent to SGs to disrupt the dynamic performance of the control system is constructed. At $t = 104.2$ s, a ramp signal with a slope of 0.01 is deliberately superimposed to P_C of SG at bus 4 over the communication link. As shown in Figure 11, ULISE estimates the received control signal, which is far away from the one sent by the MPC controller. The control signal sent by MPC is supposed to be fixed within the 104^{th} second, whilst the estimate turns out to be a monotonically increasing signal. This ULISE function enables the system operator to realize the existence of anomalies and find alternative ways of to enhance control implementation. At $t = 105.5$ s, we simulated a scenario that a mitigation scheme was initiated to tentatively disable all the communication links, and the primary controller power settings were henceforth held identical to the values at that time instant. In other words, all SGs will tentatively operate only in droop mode. The curves in Figure 11 drop to zero after $t = 105.5$ s, because the MPC controller and the ULISE are no longer operative. Other mitigation schemes, such as resending the control signals via another communication channel, could be used.

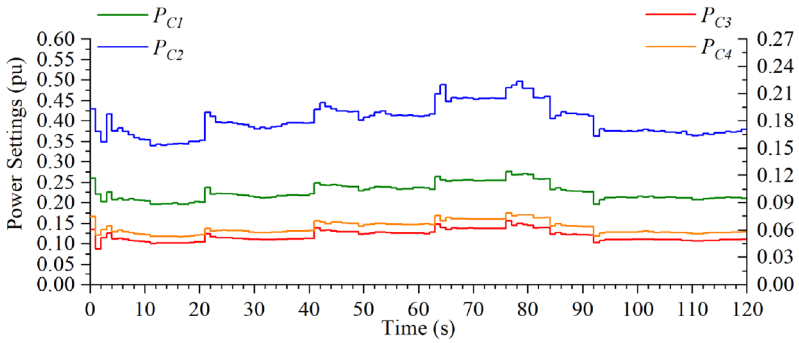

FIGURE 9 Power change settings to each SG

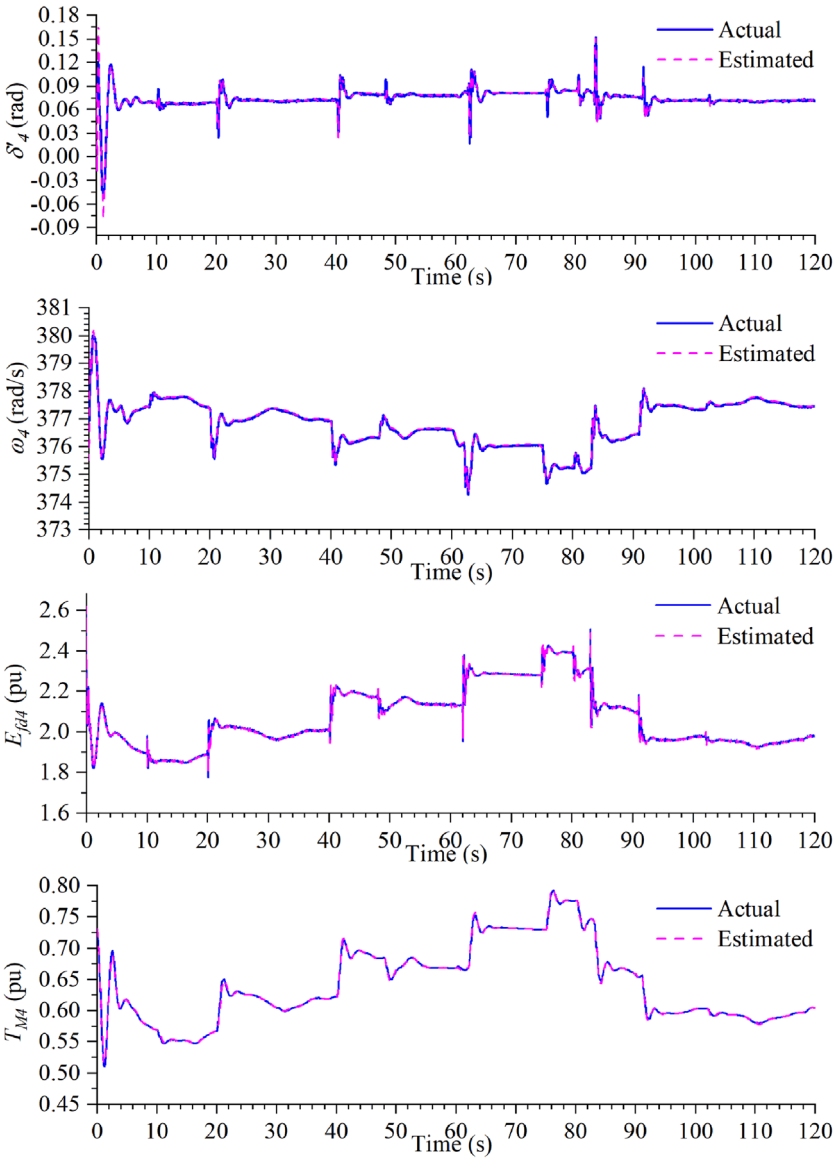

FIGURE 10 State estimation results for the SG at bus 4

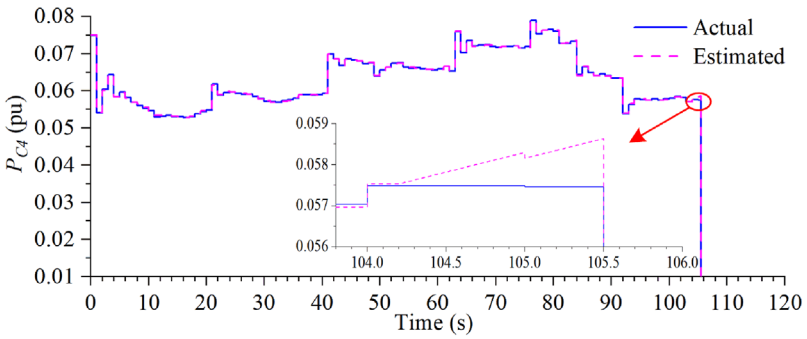

FIGURE 11 Power change setting of the SG at bus 4 under abnormal condition

Figure 12 shows the rotor angular velocity and the active power output of SG at bus 4 with and without an anomaly. Since the MPC controller is no longer operational after $t = 105.5$ s, the rotor angular velocity and the active power output tend to converge to new values dictated only by the speed-droop characteristics.

5 | CONCLUSIONS AND FUTURE WORK

In this work, an enhanced predictive hierarchical power management framework for islanded microgrids is presented. A centralized linear MPC secondary controller is designed

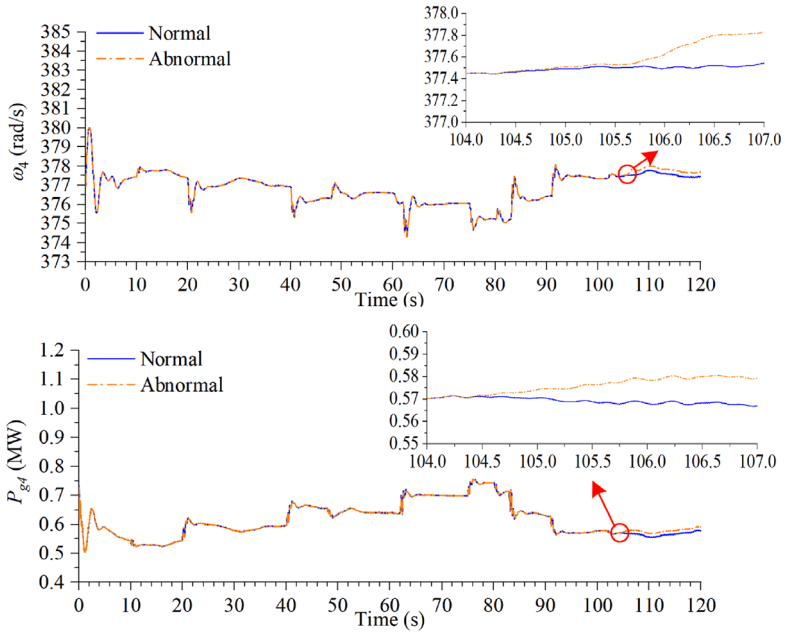

FIGURE 12 Rotor angular velocity and active power output of the SG at bus 4

for microgrid system frequency regulation and active power control. Simulation results demonstrated its consistent control performance, amid system uncertainties due to renewable generations and loads. A ULISE in a UMV sense is proposed to simultaneously estimate the system states with high precision and the actually received control signals for enhanced MPC performance. Comparing with the decentralized PI controller with well-tuned parameters, the proposed MPC controller not only brings superior frequency regulation capability but also reduces the microgrid system operating costs.

It needs to be emphasized that the MPC controller is built upon the linearized system model, which can only work well in the vicinity of a system operating point. It may not function well when large disturbances such as a fault occurs. Furthermore, the ESSs are not considered in the testing system since the renewable penetration level is relatively low compared with the total load. In the case of a higher renewable penetration, the PV system can be operated as a virtual synchronous generator to defer or even avoid the investment in ESSs while improving system stability. In our future work, a distributed stochastic nonlinear approach will be explored to explicitly model load and RESs uncertainties as MPC constraints to further improve operational efficiency.

FUNDING INFORMATION

NSF Division of Electrical, Communications and Cyber Systems, 1952683

DATA AVAILABILITY STATEMENT

The data that support the findings of this study are available from the corresponding author upon reasonable request.

CONFLICT OF INTEREST

The authors declare no conflict of interest.

NOMENCLATURE

Variables and Constants

ω_s	Nominal synchronous velocity (rad/s)
ω	Rotor angular velocity (rad/s)
δ	Rotor angle (rad)
T_M	Mechanical torque (pu)
H	Inertia constant (s)
D	Damping factor
T'_{do}	D-axis transient open-circuit time constant (s)
R_s	Stator resistance (pu)
X'_d	D-axis transient reactance (pu)
X_d, X_q	D-q axes synchronous reactances (pu)
E_{fd}, E'_q	Field winding and q-axis transient voltages (pu)
I_d, I_q	D-q axes stator currents (pu)
K_A	Combined gain of exciter and voltage regulator
T_A	Overall time constant (s) of exciter and regulator
V_{ref}	Voltage reference to voltage regulator (pu)
T_{CH}	Overall time constant (s) of turbine and governor
R_D	Droop gain
P_C	Power change setting to governor (pu)
V, θ	Bus voltage magnitude (pu) and angle (rad)
P_g, Q_g	Active and reactive powers (pu) of SG
P_D, Q_D	Aggregate active and reactive loads (pu)
P_{PV}, Q_{PV}	Active and reactive powers (pu) of PV array
P_{ref}	Economic dispatch set-point (pu) of SG
i, j	Index of Buses
θ	Bus angle (rad)
$\boldsymbol{Y}_b$	Bus admittance matrix
T_s, T_c	Model update period and control interval
N_p, N_c	Prediction horizon and control horizon

Symbols

$(\cdot)^T$	Transpose
$trace(\cdot)$	Trace

$(\cdot) \succeq 0$ Positive semi-definite matrix
$diag(\cdot)$ Diagonal matrix
$var(\cdot)$ Variance
$\mathbb{E}[\cdot]$ Expectation
$(\cdot)^{\dagger}$ Moore-Penrose pseudoinverse
$\widehat{(\cdot)}$ Estimate

ORCID

Jie Li https://orcid.org/0000-0001-6303-2307

REFERENCES

1. Vasquez, J.C., Guerrero, J.M., Miret, J., et al.: Hierarchical control of intelligent microgrids. IEEE Trans. Ind. Electron. 4(4), 23–29 (2010)
2. Bidram, A., Davoudi, A.: Hierarchical structure of microgrids control system. IEEE Trans. Smart Grid 3(4), 1963–1976 (2012)
3. Olivares, D.E., Mehrizi-Sani, A., Etemadi, A.H., et al.: Trends in microgrid control. IEEE Trans. Smart Grid 5(4), 1905–1919 (2014)
4. Diaz, N.L., Luna, A.C., Vasquez, J.C., et al.: Centralized control architecture for coordination of distributed renewable generation and energy storage in islanded AC microgrids. IEEE Trans. Power Electron. 32(7), 5202–5213 (2017)
5. Ahumada, C., Cardenas, R., Saez, D., et al.: Secondary control strategies for frequency restoration in islanded microgrids with consideration of communication delays. IEEE Trans. Smart Grid 7(3), 1430–1441 (2016)
6. Dehkordi, N.M., Sadati, N., Hamzeh, M.: Distributed robust finite-time secondary voltage and frequency control of islanded microgrids. IEEE Trans. Power Syst. 32(5), 3648–3659 (2017)
7. Deng, Z., Xu, Y., Sun, H., et al.: Distributed, bounded and finite-time convergence secondary frequency control in an autonomous microgrid. IEEE Trans. Smart Grid 10(3), 2776–2788 (2019)
8. Li, Z., Cheng, Z., Liang, J., et al.: Distributed event-triggered secondary control for economic dispatch and frequency restoration control of droop-controlled AC microgrids. IEEE Trans. Sustainable Energy. 11(3), 1938–1950 (2020)
9. Shuai, H., Fang, J., Ai, X., et al.: Stochastic optimization of economic dispatch for microgrid based on approximate dynamic programming. IEEE Trans. Smart Grid 10(3), 2440–2452 (2019)
10. Farzin, H., Fotuhi-Firuzabad, M., Moeini-Aghtaie, M.: A stochastic multi-objective framework for optimal scheduling of energy storage systems in microgrids. IEEE Trans. Smart Grid 8(1), 117–127 (2017)
11. Hosseinzadeh, M., Salmasi, F.R.: Robust optimal power management system for a hybrid AC/DC micro-grid. IEEE Trans. Sustainable Energy 6(3), 675–687 (2015)
12. Qiu, H., Gu, W., Xu, Y., et al.: Interval-partitioned uncertainty constrained robust dispatch for AC/DC hybrid microgrids with uncontrollable renewable generators. IEEE Trans. Smart Grid 10(4), 4603–4614 (2019)
13. Xiang, Y., Liu, J., Liu, Y.: Robust energy management of microgrid with uncertain renewable generation and load. IEEE Trans. Smart Grid 7(2), 1034–1043 (2016)
14. Liu, J., Chen, H., Zhang, W., et al.: Energy management problems under uncertainties for grid-connected microgrids: A chance constrained programming approach. IEEE Trans. Smart Grid 8(6), 2585–2596 (2017)
15. Li, Y., Yang, Z., Li, G., et al.: Optimal scheduling of an isolated microgrid with battery storage considering load and renewable generation uncertainties. IEEE Trans. Ind. Electron. 66(2), 1565–1575 (2019)
16. Kouvaritakis, B., Cannon, M.: Model predictive control: Classical, robust and stochastic. Springer, Cham, Switzerland (2016)
17. Mayhorn, E., Xie, L., Butler-Purry, K.: Multi-time scale coordination of distributed energy resources in isolated power systems. IEEE Trans. Smart Grid 8(2), 998–1005 (2017)
18. Jia, Y., Dong, Z.Y., Sun, C., et al.: Distributed economic model predictive control for a wind-photovoltaic-battery microgrid power system. IEEE Trans. Sustainable Energy 11(2), 1089–1099 (2020)
19. Zheng, Y., Li, S., Tan, R.: Distributed model predictive control for on-connected microgrid power management. IEEE Trans. Control Syst. Technol. 26(3), 1028–1039 (2018)
20. Delfino, F., Ferro, G., Robba, M., et al.: An architecture for the optimal control of tertiary and secondary levels in small-size islanded microgrids. Int. J. Electr. Power 103, 75–88 (2018)
21. Velasquez, M.A., Barreiro-Gomez, J., Quijano, N., et al.: Intra-hour microgrid economic dispatch based on model predictive control. IEEE Trans. Smart Grid 11(3), 1968–1979 (2020)
22. Cominesi, S.R., Farina, M., Giulioni, L., et al.: A two-layer stochastic model predictive control scheme for microgrids. IEEE Trans. Control Syst. Technol. 26(1), 1–13 (2018)
23. Lee, J.O., Kim, Y.S., Moon, S.I.: Novel supervisory control method for islanded droop-based AC/DC microgrids. IEEE Trans. Power Syst. 34(3), 2140–2151 (2019)
24. Valibeygi, A., Konakalla, S.A.R., de Callafon, R.: Predictive hierarchical control of power flow in large-scale PV microgrids with energy storage. IEEE Trans. Sustainable Energy 12(1), 412–419 (2021)
25. Ranga, V.P.S.R.V., Kesanakurthy, S.S.: Model predictive control approach for frequency and voltage control of standalone micro-grid. IET Gener. Transm. Dis. 12(14), 3405–3413 (2018)
26. Morstyn, T., Hredzak, B., Aguilera, R.P.: Model predictive control for distributed microgrid battery energy storage systems. IEEE Trans. Control Syst. Technol. 26(3), 1107–1114 (2018)
27. Ghahremani, E., Kamwa, I.: Local and wide-area PMU-based decentralized dynamic state estimation in multi-machine power systems. IEEE Trans. Power Syst. 31(1), 547–562 (2016)
28. Paul, A., Kamwa, I., Joos, G.: Centralized dynamic state estimation using a federation of extended Kalman filters with intermittent PMU data from generator terminals. IEEE Trans. Power Syst. 33(6), 6109–6119 (2018)
29. Zhou, N., Meng, D., Huang, Z., et al.: Dynamic state estimation of a synchronous machine using PMU data: A comparative study. IEEE Trans. Smart Grid 6(1), 450–460 (2015)
30. Vu, T.V., Nguyen, B.L.H., Cheng, Z., et al.: Cyber-physical microgrids: Toward future resilient communities. IEEE Ind. Electron. Mag. 14(3), 4–7 (2020)
31. Cho, S., Jiang, J.: Detection of sensor abnormalities in a pressurizer by means of analytical redundancy. IEEE Trans. Nucl. Sci. 63(6), 2925–2933 (2016)
32. McNamara, P., Milano, F.: Model predictive control-based AGC for multi-terminal HVDC-connected AC grids. IEEE Trans. Power Syst. 33(1), 1036–1048 (2018)
33. Liu, Y., Li, J., Wu, L., et al.: Chordal relaxation based ACOPF for unbalanced distribution systems with DERs and voltage regulation devices. IEEE Trans. Power Syst. 33(1), 970–984 (2018)
34. Zhang, J., Li, J., Wu, L., et al.: Hierarchical optimal control of the resilient community microgrid in islanded mode. 2019 IEEE PES General Meeting, Atlanta, GA (2019)
35. Lavaei, J., Low, S.H.: Zero duality gap in optimal power flow problem. IEEE Trans. Power Syst. 27(1), 92–107 (2012)
36. Yong, S.Z., Zhu, M., Frazzoli, E.: A unified filter for simultaneous input and state estimation of linear discrete-time stochastic systems. Automatica 63, 321–329 (2016)
37. Sauer, P.W., Pai, M.A., Chow, J.H.: Power system dynamics and stability: With synchrophasor measurement and power system toolbox. Wiley, Hoboken, New Jersey (2018)
38. Kundur, P.: Power system stability and control. McGraw Hill, New York (1994)
39. Zhang, G., McCalley, J., Wang, Q.: An AGC dynamics-constrained economic dispatch model. IEEE Trans. Power Syst. 34(5), 3931–3940 (2019)
40. Gentle, G.E.: Matrix algebra: Theory, computations and applications in statistics. Springer, Cham, Switzerland (2017)
41. Wan, C., Zhao, J., Song, Y., et al.: Photovoltaic and solar power forecasting for smart grid energy management. CSEE J. Power Energy Syst. 1(4), 38–46 (2015)

42. Chen, B., Lin, P., Lai, Y., et al.: Very-short-term power prediction for PV power plants using a simple and effective RCC-LSTM model based on short term multivariate historical datasets. Electronics 9(2), 289 (2020)
43. Visioli, A.: Practical PID control. Springer, London (2006)

How to cite this article: Zhang J., et al.: An enhanced predictive hierarchical power management framework for islanded microgrids. IET Gener. Transm. Distrib. 16, 503–516 (2022). https://doi.org/10.1049/gtd2.12297

APPENDICES A

See Tables 1-4.

TABLE A1 Line data for the 13-bus test system

From	To	r (pu)	x (pu)	b (pu)	s_{lm}^{max} (MVA)
1	5	0.00525	0.00649	0.003	5.7333
1	13	0.00330	0.00409	0.002	5.9043
2	3	0.01389	0.01718	0.007	5.6830
2	10	0.01190	0.01472	0.006	4.7878
2	11	0.01372	0.01697	0.007	0.5432
3	12	0.00064	0.00079	0.000	6.0149
4	5	0.00703	0.00869	0.003	0.3621
5	6	0.00703	0.00869	0.003	5.8439
6	7	0.00021	0.00026	0.000	6.0149
7	8	0.00567	0.00702	0.003	5.6830
8	9	0.00737	0.00911	0.004	5.0594
9	10	0.00919	0.01137	0.005	4.9286
12	13	0.00068	0.00084	0.000	5.9546

TABLE A2 Load data for the 13-bus test system

Loads	P_{DN}	Q_{DN}	a_1	a_2	a_3	b_1	b_2	b_3
L1	3.6	2.13	0.4	−0.41	1.01	4.43	−7.98	4.56
L2	3.3	2	0.38	−0.39	1.01	4.4	−7.92	4.52
L4	0.084	0.05	1.21	−1.61	1.41	4.35	−7.08	3.72
L5	0.048	0.028	0.27	−0.33	1.06	5.48	−9.7	5.22
L6	0.144	0.086	0.3	−0.42	1.12	5.39	−9.4	5.03
L7	0.054	0.031	0.55	0.24	0.21	0.55	−0.09	0.54
L8	0.504	0.299	0.76	−0.52	0.76	6.92	−11.75	5.83
L9	0.123	0.074	1.24	−1.62	1.38	4.31	−6.96	3.65
L10	0.142	0.0842	0.77	−0.84	1.07	8.09	−13.65	6.56
L12	0.048	0.0284	0.69	0.04	0.27	1.82	−2.24	1.43
L13	0.048	0.0285	0.28	−0.35	1.08	5.32	−8.9	4.59

Notes: P_{DN} is in MW and Q_{DN} is in Mvar.

TABLE A3 SG data for the 13-bus test system

DG	SG1	SG2	SG3	SG4
Rating (MVA)	3.45	6.3	0.825	0.96
H (s)	1.93	2.81	0.9	0.778
D	0.0023	0.0023	0.0015	0.0015
X_d (pu)	3.1	2.4	2.95	2.89
X_q (pu)	1.75	1.77	2.36	1.72
X_d' (pu)	0.316	0.27	0.14	0.25
T_{do}' (s)	3.5	2.3	1.7	1.46
K_A	300	300	300	300
T_A (s)	0.01	0.01	0.01	0.01
T_{CH} (s)	0.4	0.4	0.2	0.2
R_D	0.05	0.05	0.05	0.05
C_2	18.7	18.5	18.6	18.9
C_1	62	64	63	62
C_0	9	9	10	10

Notes: Per unit (pu) of reactances are based on SG power and voltage ratings.

TABLE A4 Control parameters

MPC		PI	
$g_1 = 18.94$	$g_2 = 18.94$	$P_1 = 0.07$	$I_1 = 0.0032$
$g_3 = 16.3$	$g_4 = 16.3$	$P_2 = 0.07$	$I_2 = 0.0032$
$h_1 = 0.947$	$h_2 = 0.947$	$P_3 = 0.08$	$I_3 = 0.0045$
$h_3 = 0.815$	$h_4 = 0.815$	$P_4 = 0.08$	$I_4 = 0.0045$
$\rho_\epsilon = 10^6$			